Complex force history of a calving-generated glacial earthquake derived from broadband seismic inversion

Amandine Sergeant, Anne Mangeney, Eléonore Stutzmann, Jean-Paul Montagner, Fabian Walter, Laurent Moretti, Olivier Castelnau

Complex force history of a calving-generated glacial earthquake derived from broadband seismic inversion

Amandine Sergeant[1,2], Anne Mangeney[1,2,3], Eléonore Stutzmann[1], Jean-Paul Montagner[1], Fabian Walter[4], Laurent Moretti[1], and Olivier Castelnau[5]

[1]Seismology Group, Institut de Physique du Globe de Paris, Sorbonne Paris Cité, UMR 7154, CNRS, France, [2]UFR STEP, Université Paris-Diderot 7, Sorbonne Paris Cité, France, [3]ANGE team, CEREMA, Inria, Lab. J.-L. Lions, CNRS, France, [4]Swiss Seismological Service, ETH Zurich, Zurich, Switzerland, [5]Laboratoire Procédés et Ingénierie en Mécanique et Matériaux, CNRS, ENSAM, CNAM, Paris, France

Abstract The force applied to the Earth by the calving of two icebergs at Jakobshavn Isbrae, Greenland, has been quantified. The source force history was recovered by inversion of regional broadband seismograms without any a priori constraint on the source time function, in contrast with previous studies. For periods 10–100 s, the three-component force can be obtained from distant stations alone and is proportional to the closest station seismograms. This inversion makes it possible to quantify changes of the source force direction and amplitude as a function of time and frequency. A detailed comparison with a video of the event was used to identify four forces associated with collision, then bottom-out and top-out rotation of the first and second icebergs, and ice mélange motion. Only the two iceberg rotations were identified in previous studies. All four processes are found here to contribute to the force amplitude and variability. Such a complete time-frequency force history provides unique dynamical constraints for mechanical calving models.

Key Points:
- Precise force history estimation without any constraint on the source shape
- Broadband inversion
- Complexity of the force related to different phenomena in the calving sequence

Supporting Information:
- Captions for Movie S1 and S2, Text S1, and Figures S1 and S2
- Movie S1
- Movie S2
- Figure S1
- Figure S2

Correspondence to:
A. Sergeant,
sergeant@ipgp.fr

Citation:
Sergeant, A., A. Mangeney, E. Stutzmann, J.-P. Montagner, F. Walter, L. Moretti, and O. Castelnau (2016), Complex force history of a calving-generated glacial earthquake derived from broadband seismic inversion, *Geophys. Res. Lett.*, *43*, 1055–1065, doi:10.1002/2015GL066785.

1. Introduction

Accelerated thinning and retreat of marine-terminating glaciers are examples of rapid changes affecting the Greenland ice sheet [e.g., *Thomas et al.*, 2000; *Howat et al.*, 2005; *Joughin et al.*, 2004]. They are accompanied by increasing rates of iceberg calving [*Joughin et al.*, 2004; *Howat et al.*, 2007]. Knowledge on calving processes and rates is particularly important to assess their impact on ice mass loss, tidewater-terminating glacier dynamics, and more generally on the contribution of iceberg calving to global sea level rise. However, the physical mechanisms controlling iceberg calving are not fully understood, and in situ observations are difficult to obtain.

Iceberg calving generates glacial earthquakes [e.g., *Joughin et al.*, 2008; *Nettles et al.*, 2008; *Amundson et al.*, 2008; *Nettles and Ekström*, 2010; *Veitch and Nettles*, 2012] which can be recorded from local to teleseismic distances [e.g., *Amundson et al.*, 2008; *Veitch and Nettles*, 2012]. Therefore, seismic data provide useful information for understanding and quantifying iceberg calving dynamics and the physical processes at work as well as for monitoring calving events at global distances. In addition, the availability of continuous seismic records should make it possible to track back past events and assess mass loss fluctuations over long time scales.

Glacial earthquakes are a class of calving-generated seismic events of magnitude ~5 [e.g., *Nettles and Ekström*, 2010]. They are located primarily in Greenland, in the margins of large marine-terminating glaciers with near-grounded termini. They occur during the calving of cubic-kilometer scale unstable icebergs of the full-glacier thickness [e.g., *Murray et al.*, 2015]. Those calving events are driven by the buoyancy forces that capsize the resulting iceberg against the calving front and along the bottom of the fjord. These phenomena produce long-lasting seismic sources that can be recorded in the long-period band 10–150 s. Despite significant recent advances in their understanding, the precise source mechanisms and their relative contribution are still subject to debate. The earthquake is assumed to be generated by the iceberg scrapping the fjord bottom [*Amundson et al.*, 2008] or colliding the terminus. Seismic waves may be generated by the eventual rebound of the iceberg on the calving front once it has capsized [*Walter et al.*, 2012] or by the contact force applied on the terminus during the ~5 min long iceberg overturning process [*Amundson et al.*, 2008; *Tsai et al.*, 2008; *Walter et al.*, 2012]. As the iceberg capsizes, it pushes and compresses the glacier front elastically and

causes reversal of the glacier's horizontal flow [*Murray et al.*, 2015]. The glacier then rebounds toward the fjord as its contact with the overturning iceberg is relaxed. Additionally, the water pressure drop behind the capsizing iceberg may cause a downward motion of the glacier terminus resulting in an upward force on the solid Earth [*Murray et al.*, 2015].

Despite the complexity of the source mechanisms, previous studies modeled these icequakes as a single process using simple predefined forces [*Ekström et al.*, 2003]. In particular, *Tsai and Ekström* [2007] successfully modeled teleseismic waveforms in the 40–150 s period band using a centroid single force model (double boxcar or CSF model). The CSF model essentially imposes a constant force axis, found to be nearly horizontal, as well as equal positive (i.e., in the upglacier direction) and negative (downglacier direction) boxcar durations and amplitudes. The best fitted model gives a total source duration of about 50 s corresponding to the dominant period of the seismic signal.

Walter et al. [2012] analyzed the glacial earthquake generated at Jakobshavn Isbrae in Greenland on 21 August 2009. By comparing time-lapse images of the calving episode with seismograms recorded nearby, they identified the signal generated by the rotation of two nearby icebergs. They also modeled regional seismograms considering a CSF source model and other single force models such as simple boxcar and delta functions. In the 10–20 s narrow period band inverted in *Walter et al.* [2012], seismic waveforms are equivalently well fitted by either source model. However the magnitude of the event is highly variable depending on the choice of the source time function. As a result, their source amplitude cannot be used to quantify dynamical processes or estimate the iceberg volume.

CSF source models have also been used to model seismic signals generated by landslides [*Kawakatsu*, 1989; *Zhao et al.*, 2014]. However, in landslide seismology, the source force is commonly obtained by seismogram inversion without any a priori constraint on the force history [e.g., *Brodsky et al.*, 2003; *Moretti et al.*, 2012, 2015; *Yamada et al.*, 2013]. These studies have shown that the force applied by the landslide to the ground is more complex than its description in the CSF model. In particular, the force history reflects the interaction of the flow with topography fluctuations and the resulting centrifugal accelerations [*Moretti et al.*, 2012, 2015; *Levy et al.*, 2015]. The inverted force provides a unique tool to discriminate between different dynamical landslide models and quantify the physical and mechanical processes at work along with the associated rheological parameters [e.g., *Yamada et al.*, 2014; *Levy et al.*, 2015]. Similarly, in the complex environment of tidewater glacier termini, glacial earthquakes are expected to result from the combination of several processes which may interact and generate a complex force history, richer than that contained in the CSF model.

In this paper, we invert seismograms generated by the well-documented glacial earthquake of 21 August 2009 [*Amundson et al.*, 2010; *Walter et al.*, 2012]. In contrast with previous studies, we make no assumptions on the source model, other than that it is a single 3-D force, and we invert signals in the 10–100 s wide period band. By choosing alternatively nearby (57 km from the source) and distant stations (>250 km), we show that the inverted force history is very stable and can be obtained from distant stations alone. We observe that the three components of the inverted force are, respectively, proportional to the three components of the seismograms recorded close to the glacial earthquake. This inversion makes it possible to quantify the variability of the force direction and amplitude in time and frequency, which appears to be much more complex than its representation in the CSF model. By comparing the force time-frequency history with time-lapse images of the calving episode, we identify four forces that occur simultaneously and are thus possibly associated with the (1) collision and (2) bottom-out rotation of the first iceberg, (3) top-out rotation of the second iceberg, and (4) ice mélange motion. Although only the two iceberg rotations have been identified in previous studies, we show that all four processes are necessary to quantitatively explain the variability of the force direction and amplitude.

2. Description of the Calving Event and Seismic Data

We focus on the large-scale multiple-iceberg calving episode that occurred at the terminus of the Jakobshavn Isbrae on 21 August 2009. It was recorded by broadband seismic stations located in Greenland. We use seismic records from four permanent stations of the GLISN network [*Clinton et al.*, 2014], ILULI, SFJD, SUMG, and KULLO, located, respectively, 57, 247, 556, and 661 km from the calving zone (Figure 1a). We also use data from a broadband station (WIND) which was temporally installed on the bedrock 4 km from the source area. Seismic records are down sampled to 1 Hz. The mean and trend are removed from the time series prior to correction of the instrumental response, then the records are integrated to obtain ground displacement.

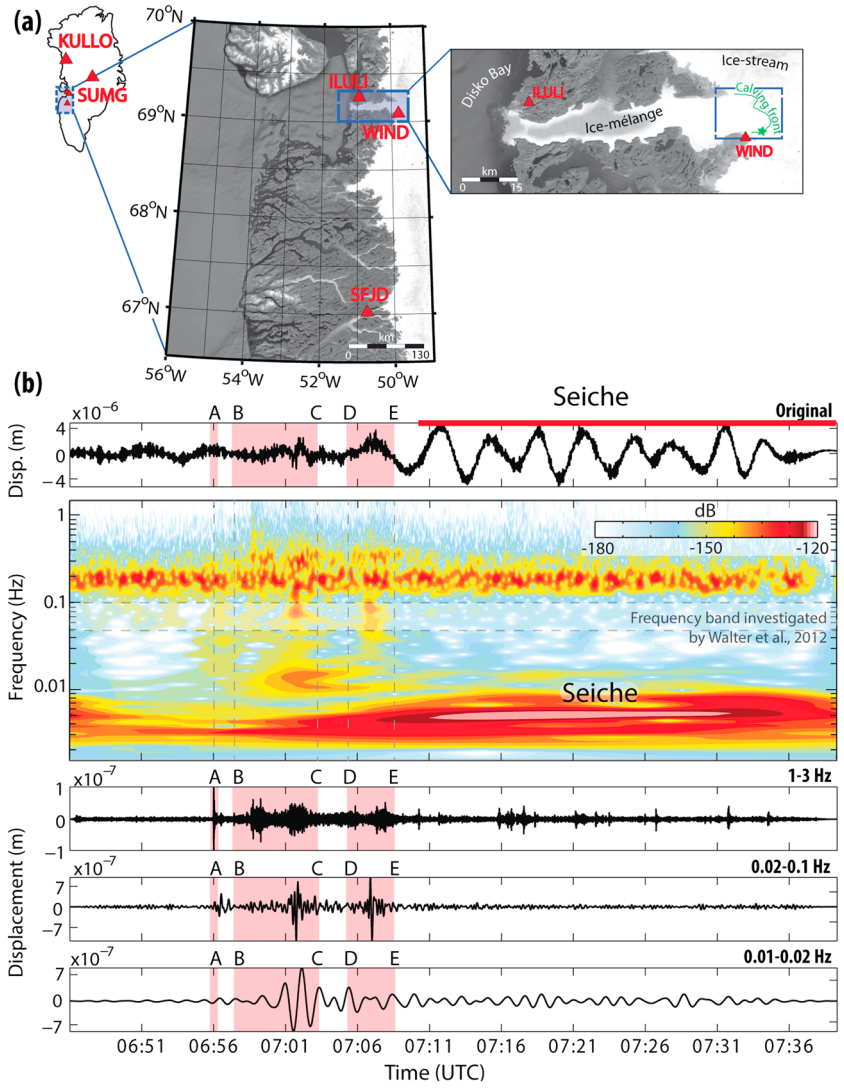

Figure 1. (a) Seismic station locations (red triangles) on Google Earth images of the west coast of Greenland and the Jakobshavn Isbrae, its terminus, and its proglacial fjord. The green star indicates the calving event location. (b) Vertical ground displacement at ILULI and associated spectrogram. Original seismogram, spectrogram, and band-pass-filtered records, 1–3 Hz (0.33–1 s), 0.02–0.1 Hz (10–50 s), and 0.01–0.02 Hz (50–100 s), from the top. Time-lapse images have been used to link the generation of seismic bursts to the calving event sequence: (A) the ice avalanche along the flank of the first iceberg to be calved; (B–C) the capsizing of the first iceberg from the vertical position in contact with the terminus to the horizontal position detached from the terminus; (D–E) same as B–C but for the second iceberg.

Figure 1b shows the vertical displacement and associated spectrogram at ILULI, located at the mouth of the Jakobshavn fjord. In order to interpret the seismic signal, we compare it with synchronized 10 s images of the event, recorded by a camera colocated at WIND station. Such a comparison was made by *Walter et al.* [2012] in the two narrow frequency bands of 1–3 Hz and 0.05–0.1 Hz. Here we analyze the complete seismic signal between 0.001 Hz and 3 Hz, making it possible to better identify the broad frequency range associated with each source mechanism (i.e., each subevent). Data are shifted backward by subtracting the travel time for Rayleigh waves to propagate from the source to the receiver, assuming a velocity of 4.36 km/s [*Walter et al.*, 2012]. Movie S1 in the supporting information shows the calving episode viewed from WIND station and the synchronized seismograms.

The calving event initiated at 06:56:31 UTC with a slump of a large ice slab which slips down from the ice front of the terminus into the fjord (time A in Figure 1b). It occurs at the same time as the generation of an impulsive high-frequency seismic signal peak (1–3 Hz) and a lower frequency emergent 100 s long signal (0.02–0.1 Hz).

The ice slump was directly followed by small amplitude motion of the ice mélange in the source area and emission of seismic energy at high (1 – 3 Hz) and low (0.01 – 0.02 Hz) frequencies. The calving and bottom-out rotation (i.e., the top of the iceberg moves toward the glacier) of the full-glacier-thickness iceberg with a volume of about 0.45 km^3 occurred during the time period indicated by B – C in Figure 1b. It was directly followed by the calving and the top-out rotation (i.e., the top of the iceberg moves away from the local front) of a second smaller (by approximately a factor 3) iceberg (time period D – E). These two phenomena produced seismic energy in a wide frequency range down to 0.01 Hz and distinct bursts of seismic signal only at frequencies $\geq$0.02 Hz.

We observe bursts and peaks with high-frequency energy (1 – 3 Hz) throughout the entire event duration (after time A in Figure 1b). They occur while the ice mélange moves in the proglacial fjord and accelerates away from the terminus as the rotation of the icebergs displaces massive amount of water. *Amundson et al.* [2010] analyzed continuous seismic signals in the Jakobshavn fjord and associated the numerous high-frequency bursts with ice mélange fracturing. Fracturing of the ice mélange is probably also the source of the high-frequency signals observed in Figure 1b.

Finally, the raw seismogram shows a very low frequency ($\leq$0.01 Hz) seismic signal $\sim$10 min after the onset of the calving. This signal lasts for 30 min and represents ground tilt induced by ocean waves which travelled along the 50 km long fjord from the calved area to the ocean at the fjord resonance frequencies (seiche). It was observed only at the nearby coastal station ILULI. Similar long-period seismic signal related to seiche and recorded at close and coastal stations has been observed for many calving events at various glaciers by *Amundson et al.* [2012a] and *Walter et al.* [2013].

Comparison between a video and the broadband seismic signal recorded near the event enabled us to identify several phases in the seismic signal with different frequency content, possibly related to the complicated calving history. The spectrogram generated by this complex source can most likely not be explained by a single process with an acceleration and deceleration phase along a constant direction as assumed in a CSF source model. In the next sections we invert seismograms without any a priori constraint on the source model and we then interpret the complex inverted force.

3. Source Inversion

3.1. Method and Green's Function Calculation

As for landslides, we assume that the seismic source of glacial earthquakes can be modeled as one or several forces rather than a moment tensor like for tectonic earthquakes. As in *Moretti et al.* [2012, 2015] and *Yamada et al.* [2013], we perform a waveform inversion in the frequency domain to obtain the force-time function of the event. Prior to the inversion, data are filtered using a zero-phase fourth-order Butterworth filter (0.01 and 0.1 Hz). These corner frequencies are determined on the seismic signal frequency band. The upper frequency limit comes from the difficulty to compute accurate Green's functions for periods lower than 10 s which are much more sensitive to 3-D structural heterogeneities. Because we are interested in the calving process rather than the seiche episode, we select the lower frequency of 0.01 Hz. Each data component is then down weighted based on its signal-to-noise ratio. We finally invert nine seismograms excluding the horizontal components of WIND, SUMG, and KULLO because of their strong long-period background noise. The *i*th component of the displacement $\mathbf{u}_i(x,t)$ recorded at a distance x from the source can be written

$$\mathbf{u}_i(x,t) = \mathbf{g}_{ij}(x,t) * \mathbf{f}_j(0,t), \tag{1}$$

where t is the time, $\mathbf{f_j}(0,t)$ is the force at location 0 along the direction j ($j = E, N, Z$), and $\mathbf{g}_{ij}(x,t)$ is the Green's function for the seismogram component i and force component j. The symbol $*$ denotes the convolution product. Equation (1) can be rewritten, in matrix form in the frequency domain

$$U(\omega) = G(\omega)F(\omega), \tag{2}$$

where U, G, and F are the Fourier transforms of $\mathbf{u}$, $\mathbf{g}$, and $\mathbf{f}$, respectively. The solution in the least squares sense for the force-time function is given by

$$F = (G'G)^{-1}G'U, \tag{3}$$

where $'$ is the conjugate transpose. We then perform an inverse Fourier transform on the solution to obtain the three-component force time history.

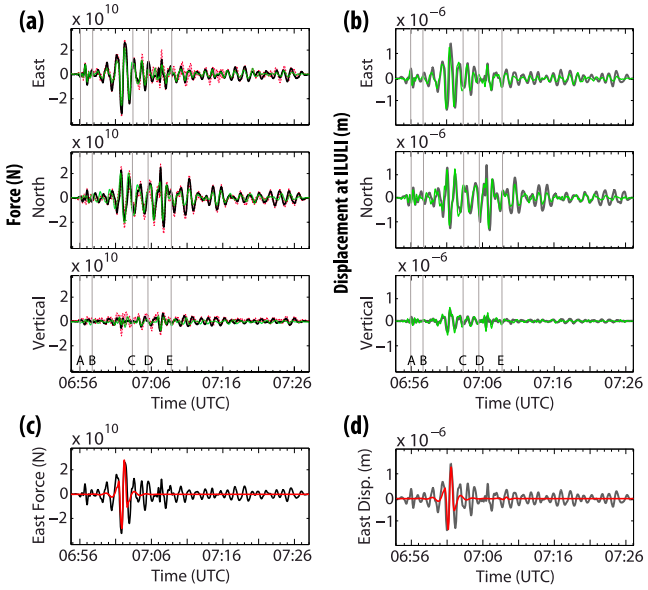

Figure 2. (a) 0.01–0.1 Hz band-passed force-time function from inversion of seismic data from all stations (black line) and using only four components from distant stations SFJD, SUMG, and KULLO (green line), along with the 95% confidence interval of the solution estimated using the jackknife method (pink area). (b) The 0.01–0.1 Hz band-passed data (gray line) and synthetic seismograms (green line) at station ILULI. (c) Force fit with the 0.01–0.1 Hz filtered CSF model inverted by *Veitch and Nettles* [2012]. The east components of the force and the CSF function are in black and red, respectively. (d) Ground displacement waveform fits for the 0.05–0.1 Hz seismic signals recorded on the east component of ILULI. Data are in gray. The synthetic seismogram based on the CSF model is in red. Marks A to E are the same as in Figure 1.

Green's functions are calculated using the discrete wave number method [*Bouchon*, 1981] used in *Favreau et al.* [2010]. The forces are assumed to occur at the Earth surface so are modeled the Green's functions. The 1-D velocity model is given by *Walter et al.* [2012]. This model is based on crust2.0 for the crustal layers [*Bassin et al.*, 2000]. We combine it with the preliminary reference Earth model for layers deeper than 37 km [*Dziewonski et al.*, 1981]. The source location is fixed and was derived from Landsat imagery by *Walter et al.* [2012] with a 1 km uncertainty. The two icebergs did not calve from the exact same position (less than 1 km of horizontal uncertainty). However, given the considered frequency range (0.01–0.1 s), the source location difference has a negligible influence on the inverted force.

Time uncertainties are partly due to the use of a 1-D Earth model for modeling the seismic wave propagation. Thus, the synthetic waveforms cannot be expected to perfectly align with the observed seismograms for each component. This primarily results from errors in lateral seismic velocity variations, changes in the ice layer thickness especially at SUMG, and possibly seismic anisotropy in the ice [*Wittlinger and Farra*, 2014]. The time lag (τ lag) between data and the synthetic waveforms is computed by cross correlating the recorded and modeled waveforms at each station individually. The initial Green's functions are shifted by the corresponding τ value which varies from a few to ~20 s depending on the source station path. Finally, the inversion scheme is repeated a second time. With respect to the initial inversion, the source origin time is shifted by 2 s but the general shape of the source is the same at both iterations, indicating a certain robustness of the method.

3.2. Stability of the Inverted Force and Uncertainty

The resultant source time functions for the three force components are shown in Figure 2a. Since the observed waveforms were filtered between 0.01 and 0.1 Hz, the inverted source (black line) is band-passed in the same frequency range. To test the stability of the inversion, we use the jackknife technique [*Quenouille*, 1956; *Tukey*, 1958] which consists in constructing a robust confidence interval estimation of the model by using subsets of available data in the inversion. We construct a 95% confidence interval of the solution (pink area) using 2 standard deviations of the 50 inverted forces. The uncertainty lies mainly in the absolute amplitudes, while the overall shape of the force is stable. At each time interval, the relative amplitude uncertainty is similar on each force component so that we can reliably use this inverted source to study the force direction variation.

To assess the influence of the nearby stations on the final force result, we also invert the force using only stations at distances greater than 250 km from the source. The forces inverted with all stations (black line) and with the most distant stations only (green line) show little difference, proving the robustness of the inversion result.

Figure 2b shows the good fit between observed (gray line) and synthetic seismograms (green line) at the nearby three-component station ILULI (57 km). The synthetic seismograms are calculated by the convolution of the Green's functions with the source inverted with distant station records only, i.e., without ILULI (green line, Figure 2a). We also observe that if normalized, the inverted force and the ground displacement waveforms at ILULI are very similar. This implies that at this distance and in this frequency range, propagation effects can be considered constant and the normalized seismic waveforms at the nearby station directly describe the normalized force history. This implies that in radial-transverse-vertical (RTZ) components, force amplitude should linearly scale the displacement amplitude at nearby stations, as long as the force has a constant direction, i.e., radial axis. Waveform inversion is nevertheless necessary to obtain the force direction and amplitude in newtons.

Finally, we note that the synthetic seismograms do not fit amplitude data well after 07:11 UTC especially on the north component, as the long-period (>50 s) seismic signal at ILULI also contains seiche-induced ground tilt (Figure 1b). This is only recorded at this coastal station and has maximum amplitude on the north component. In the next section we interpret the inverted force.

4. Inverted Force Analysis

The single force displays a high variability in time and frequency. Figure 3 shows (a) the spectrograms of the E-W, N-S and vertical forces and (b) the force time functions filtered in two frequency bands 0.02–0.1 Hz (10–50 s) and 0.01–0.02 Hz (50–100 s). Movie S2 shows the force history synchronized with the time-lapse photography of the event and the displacement computed every 10 s in unit of pixel of the camera detector. We identify four phases in the force history, which have different magnitudes, durations, and energy distribution over frequency which are described hereafter.

4.1. Forces Related to Iceberg Capsizing

Forces (1) to (3) are similar in terms of duration (~2 min long), order of magnitude ($\times 10^{10}$N), frequencies of maximum energy (0.02–0.1 Hz), and polarity. They are coincident with overturning of icebergs in the source area. Their characteristics and origins are discussed below.

4.1.1. Force (1) Related to the Initiation of One Iceberg Capsize

Force (1) is 100 s long and has maximum energy between 0.025 and 0.1 Hz (10–40 s) over the investigated frequency band (0.01–0.1 Hz) (Figure 3). This force was not investigated in the study of *Walter et al.* [2012] which involved higher frequencies. The maximum force amplitude is 0.5×10^{10} N. It is near horizontal with a horizontal/vertical (H/V) ratio equal to 6.7. Its particle motion in the horizontal plane (Figure 3c) shows that the force is linearly polarized for the first 50 s and has a stable azimuth. The force direction (arrow (1) in Figure 3d) is normal to the precalving front (black line) with an azimuth of 127° and a dip of 2°.

This force coincides in time with the ice slumping along the front of the first iceberg to capsize. The force dip does not coincide with what would be expected for the sliding of ice debris down along the near-vertical calving front. Indeed, as for landslides, the acceleration and deceleration of a rigid mass that slides down a slope creates a force parallel to the sliding surface in the flow direction and lasting the whole slip duration. While the force azimuth of 127° is perpendicular to the calving front and therefore in the avalanche flow horizontal direction, the dip of 2° is much too small and would have been expected to be around 90°. The slab is actually slipping down the ice front of the first large iceberg which may be already detached from the glacier and is about to capsize. Indeed, *Amundson et al.* [2010] suggest that small rotation at the terminus (below 1°) may be sufficiently large to cause near-terminus icebergs that subtly shift their positions and then trigger avalanching or collapses of large mass of ice into the surrounding water. Besides, by investigating high-frequency signals (≥1 Hz) generated in several glaciers in Greenland and Alaska, *Amundson et al.* [2010] and *Walter et al.* [2010] interpreted the bursts before calving episodes as the result of rift propagation or widespread fracturing of the ice block about to be calved from the terminus. While these processes may be the source of the large high-frequency signal observed at time A in Figure 1, we do not consider it to be possible that they could generate this lower frequency force (1). Indeed, only high-frequency seismic signals (>1 Hz) have been associated with those phenomena [*O'Neel et al.*, 2007; *Rial et al.*, 2009; *Walter et al.*, 2009, 2010; *Heeszel et al.*, 2014].

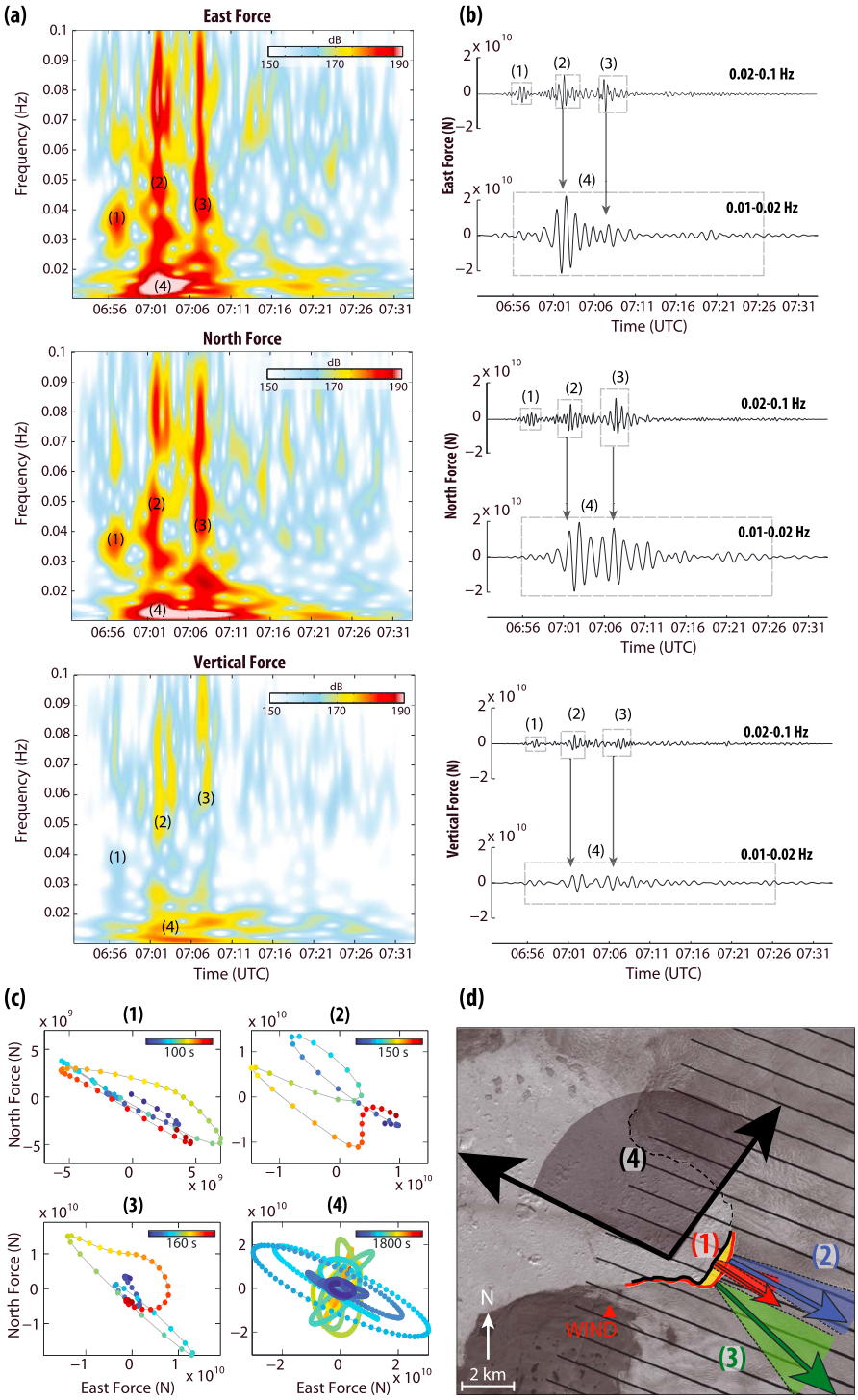

Figure 3. (a) Spectrograms of the force-time function. (b) Force-time function band-pass-filtered between (top) 0.02 and 0.1 Hz and (bottom) 0.01 and 0.02 Hz. (c) Filtered force motion in the horizontal plane for the four time windows indicated in Figure 3b. The points are colored with respect to the relative time of each event. (d) Landsat image of the Jakobshavn Isbrae terminus before (14 August 2009) the calving episode (21 August 2009). The black curves (thick and dashed) indicate the precalving front position. The red curve indicates the terminus position after the calving event, derived from Landsat imagery (23 August 2009). The calved area is shown in yellow. The colored arrows and arcs indicate the force directions and their variation over time, estimated for (1) the ice avalanche along the first iceberg to be calved, (2) the first and (3) the second iceberg calvings, and (4) the motion in the proglacial fjord. The arrow length is proportional to the associated force amplitude. Note that the force direction can have a 180° ambiguity which cannot be resolved by our polarization analysis.

Moreover, such fracturing processes have been shown to produce signals with lower amplitudes than those observed here [*Bartholomaus et al.*, 2012]. We therefore associate force (1) with processes related to the initiation of the iceberg overturning. The ice slab slumping is driven by the motion of the first large iceberg as it begins to rotate against the terminus (Movies S1 and S2). The force resulting from ice slipping would then be transmitted to the solid Earth through the contact between the rotating iceberg and the terminus, leading to an almost horizontal force (see section 4.1.2).

Another possible explanation is that the force is associated with a collision or a modification in the contact between the iceberg and the terminus. Due to the ice slump at the front, the large detached iceberg has lost mass, and therefore, its buoyancy state may have been changed. This should result in a balancing of the rotating mass position and would possibly lead to a change in the rotation dynamics and the contact with the calving face. During this balancing process, the ice block could impact the terminus with a small tilt angle producing a force normal to the terminus at the contact location [*Murray et al.*, 2015; *Sergeant et al.*, 2015]. The more the iceberg is tilted, the higher the iceberg kinetic energy and the higher the resultant external force applied on the terminus [*Amundson et al.*, 2012b; *Sergeant et al.*, 2015].

4.1.2. Forces (2) and (3) Related to Capsizing-Iceberg-to-Terminus Contact

Forces (2) and (3) have high energy over the entire frequency band 0.01–0.1 Hz (Figure 3). The two pulses are particularly distinguishable for frequencies higher than 0.02 Hz and have similar durations of about 150 s and magnitudes around 1×10^{10}N in the 0.02–0.1 Hz range. Both forces are linearly polarized for the first half of their duration (Figure 3c). Force (2) has an H/V ratio of 3.5. Its azimuth varies from 110° to 140° and the averaged azimuth is 122°. Force (2) dip also varies from 3° to 13°. Force (3) has an azimuth of about 135°, and its H/V ratio is 6.7 which corresponds to a small dip which varies from 3° to −1°.

Forces (2) and (3) are associated with the capsizing of the first and second icebergs, respectively. The two forces are perpendicular to the postcalving front (red line, Figure 3d) at the approximate iceberg location. These two forces are consistent with those obtained by *Walter et al.* [2012] in the narrower 0.05–0.1 Hz frequency band (Figure S1) and by *Veitch and Nettles* [2012] who modeled the seismic signals at lower frequencies (0.006–0.03 Hz) as a single iceberg capsizing event (see section 5). Forces (2) and (3) result from the contact between the terminus and the icebergs as they capsize. On the contrary to force (1), these forces occur near the release of the contact (Movie S2), simultaneously or right after the transition in the terminus motion direction from upglacier to downglacier [*Murray et al.*, 2015; *Sergeant et al.*, 2015].

Despite the large difference in size of the two icebergs, the associated 0.02–0.1 Hz forces have similar amplitudes, durations, and energy. The first iceberg calved bottom-out forcing the ice mélange to accelerate away from the terminus (Movie S2), reducing the resistive force that the ice debris cover can apply on the calving front. This allows other smaller icebergs to calve subsequently top out from the terminus [*Amundson et al.*, 2010], as observed here. From laboratory experiments, *Amundson et al.* [2012b] showed that top-out capsizing icebergs release more kinetic energy than bottom-out capsizing icebergs of the same size possibly because hydrodynamic forces have a greater effect on top-out than on bottom-out iceberg capsizing. They also showed that the water pressure gradients greatly increase the magnitude of the iceberg-terminus contact force. Therefore, icebergs that capsize top out may exert larger forces on the terminus than icebergs that capsize bottom out. This may explain why we have obtained similar force amplitude and frequency content for the large iceberg that capsized bottom out and the smaller iceberg that capsized top out.

4.2. Force Related to the Ice Mélange Motion

The last force, force (4), is initiated right after the ice avalanche and lasts throughout the event duration, i.e., about 20 min. This is the first time that such a long-duration force associated with a calving event has been quantified. It has energy between 0.01 and 0.02 Hz. Movie S2 shows the synchronized three-component force time series, the time-lapse imagery, and the pixel horizontal and vertical displacements of the mélange during the event. This was done by cross correlating each pixel from right to left or bottom to top directions between each original frame (Computation done by J. Amundson, private communication, 2015). The maximum amplitudes on horizontal components of the 0.01–0.02 Hz filtered force coincide with the capsizing of the two icebergs (2.1×10^{10}N and 1.8×10^{10}N, respectively), and a part of the signal may be associated with rotation of the calved blocks (section 4.1.2). The force magnitude drops after 07:16 UTC, when the mélange amplitude motion starts to decrease in the margins of the calving area and stops after 07:26 UTC (Movie S2).

interaction of several single forces which cannot be resolved individually or be related to a more complex physical process which cannot be described by single forces. The force H/V ratio is 7.7 and the dip is less than 2°. The force azimuth varies over time from 120° to 50°. Figure 3d shows the corner azimuths of the force with directions varying from normal to parallel to the calving front in the source area (Figure 3d).

The full-event duration (∼20 min) suggests that at least part of force (4) results from the ice mélange motion in the vicinity of the calved area. Visual observations of the Jakobshavn proglacial ice mélange suggest that the mélange forms a semirigid, viscoelastic cap extending over ∼20 km from the terminus along the fjord. This implies that its motion can be accommodated by deformation and/or slip in narrow shear bands within and along the margins of the mélange [*Amundson et al.*, 2010]. Furthermore, *Peters et al.* [2015] measured a jamming front velocity of about 20 m/s. It reaches the other side of the fjord within a minute which is a negligible time delay compared to our force duration. As the front then propagates along the fjord, it applies shear forces along the fjord walls. This is in good agreement with the multiple directions of the seismic source. The role of the ice mélange in calving events has also been investigated by *Tsai et al.* [2008]. In order to reproduce analytically the amplitude of the force generated by a calving event, they had to include the resistive forces generated by the ice mélange which can be transmitted from block to block across kilometers in the proglacial fjord with little time delay [*Truffer et al.*, 2006]. Based on these previous studies and the characteristics of the 0.01–0.02 Hz inverted force (4), we interpret this as a succession of near-horizontal colliding or shear forces which act (1) along the margins of the terminus and/or (2) within the mélange.

5. Comparison With the CSF

Let us compare the force discussed in the previous section (hereafter called TF for total force) with the CSF. The CSF corresponds to the force associated with one acceleration and one deceleration of the iceberg, that is, two forces of opposite directions, equal in duration but shifted in time. The CSF is computed for the source parameters inverted by *Veitch and Nettles* [2012] (i.e., centroid time t_0 = 07:02:19 UTC, total duration T = 50 s, constant azimuth $\alpha = 119°$ with respect to the north and dip $\delta = 11°$ with respect to the horizontal). The CSF is then filtered in the frequency band of interest, i.e., 0.01–0.1 Hz. Figure 2c shows both the TF and CSF. Note that the maximum force amplitude is similar for both forces. The CSF source duration is shorter and reproduces only part of the TF. Figure 2d shows the East component of the observed and modeled seismic waveform recorded at station ILULI. The CSF seismogram do not reproduce the waveform, whereas Figure 2c shows a good fit between data and the TF synthetic seismogram.

Walter et al. [2012] successfully modeled the 0.05–0.1 Hz (10–20 s period) seismic waveforms with delta and CSF functions. In this narrow frequency band, the successive capsizing of the two icebergs generates two distinct seismic bursts (Figure 1b). Each of them can be modeled by a single source force that describes either iceberg-to-terminus collision or the glacier elastic rebound induced by the rotating iceberg-to-terminus contact force [*Murray et al.*, 2015]. When filtered in the 0.05–0.1 Hz frequency band, there is a good agreement between the TF and that obtained by *Walter et al.* [2012] (Figure S1a); however, the seismogram waveform and amplitude are better fitted with the TF force (Figure S2).

The inverted force displays strong oscillations which result from data filtering effects. Figure S1a show the normalized best fit models of CSF (blue) and those models filtered in the period band of interest (red). The filtered CSF displays the same oscillations as the ones we inverted and also the same main axis of motion (red line in Figure S1b). The changes of direction within few degrees we measure from the inverted force are then not artifacts from filtering. *Murray et al.* [2015] and *Mac Cathles et al.* [2015] measured laboratory-scale contact forces produced by the buoyancy-driven capsize of plastic blocks against a wall. Varying the capsizing block aspect ratio changes the slopes of the force during the contact, especially when it decreases, that corresponds to the generation of glacial earthquake seismic signals (forces 2 and 3). Those changes will affect the force history and cannot be modeled by symmetric CSF. Even though oscillations of the force are nonphysical, their relative amplitudes provide important constraints on the event dynamic.

6. Discussion and Conclusion

We have inverted the source force responsible for the generation of low-frequency (0.01–0.1 Hz) seismic signals associated with a well-documented two-iceberg calving event. The three components of the force inverted from either distant or nearby stations are proportional to seismic waveforms recorded at the closest station (∼50 km). As a result, at this station, the normalized force history can be directly seen on the seismic

signal itself, making it possible to track the different processes at work, without perturbations due to propagation effects. In this frequency range, force and displacement amplitudes at nearby stations should then scale with each other in the RTZ directions of the force and this across all calving events.

Thanks to the inversion, we quantify for the first time the change in time of the amplitude and direction of the force. We identify and characterize new source processes with distinct frequency contents, durations, and amplitudes. They are related to different mechanisms which can occur successively or simultaneously. They all play a significant role in the generated seismic signal. This demonstrates that a calving-generated seismic signal cannot be modeled with a single source process, and this inversion procedure enables to retrieve rapidly and accurately the force characteristics for every signal frequency.

Veitch and Nettles [2012] analyzed the size distributions of 121 glacial earthquakes at various outlet glaciers in Greenland and suggested that each glacier is characterized by a size frequency distribution with a characteristic shape and peak dependent on its size and geometry. Under the assumption that each glacier may produce a wide range of iceberg size, this implies that the distribution of glacial earthquakes magnitudes should be as much affected by one glacier characteristics rather than the calved iceberg size distribution. Our results show that regarding the interpretation of glacial earthquakes as being generated by one single force resulting from iceberg capsizing, the seismic magnitude is not related to the iceberg volume in a simple manner. In particular, we show that at frequencies lower than 0.02 Hz, the absolute amplitude of the force results from the interaction of two distinct source processes: (1) the contact force induced by the rotation or collision of the capsizing iceberg and (2) shear forces along the fjord wall induced by the ice mélange motion. The coda of this low-frequency force represents the ice mélange motion only. Its amplitude therefore sets a lower bound on the amount of the 0.01 – 0.02 Hz force magnitude resulting from motion of the mélange only. In addition, glacial earthquake magnitude depends on the grounded state of the terminus [e.g., *Tsai et al.*, 2008] as well as the glacier and fjord size and geometry [*Veitch and Nettles*, 2012], the calving style, the presence of nonlinear hydrodynamic drag forces which affect the iceberg rotation dynamic [*Burton et al.*, 2012; *Amundson et al.*, 2012b], and the ice mélange stiffness which strongly influences iceberg calving style and iceberg-terminus contact forces [*Tsai et al.*, 2008; *Amundson et al.*, 2010]. All these factors may strongly affect the force history, amplitude, and energy distribution. Estimating iceberg size from the absolute amplitude of the force is therefore not straightforward because of the complex environment and the contribution of multiple source processes. Our study has made it possible to quantify the respective roles of the different physical processes at the origin of the glacial earthquake at Jakobshavn Isbrae (21 August 2009).

The inverted force history represents a unique dynamical constraint to discriminate between different mechanical models of calving events and to quantify the associated rheological parameters. This force can be obtained from distant stations that have recorded these events over several tens of years so that our method could help to track back the changes of the different processes involved in iceberg calving dynamics over this whole period.

Acknowledgments

We thank the operators of the Greenland Ice Sheet Monitoring Network (GLISN) and IRIS/IDA for collecting and providing the broadband seismic data used in this study (www.iris.edu). We thank V. Yastrebov for fruitful discussions about mecanical processes. We acknowledge J. Amundson, M. Fahnestock, and M. Truffer from the University of Alaska Fairbanks for providing the time-lapse sequence of the mélange pixel displacement. To access the original frames of the time-lapse sequence, please contact J. Amundson (jason.amundson@uas.alaska.edu). We thank Martin Vallée for the fruitful discussions on inversion methods and A. Mordret for the constructive comments on an earlier version of the manuscript. We also thank T. Bartholomaus for the reviews which greatly helped to improve this manuscript. This work has been partially funded by the ANR contract ANR-11-BS01-0016LANDQUAKES, CNCS-UEFISCDI project PN-II-ID-PCE-2011-3-0045, and the ERC contract ERC-CG-2013-PE10-617472 SLIDEQUAKES. The research was supported by a DGA-MRIS scholarship. This is IPGP contribution 3706.

References

Amundson, J. M., M. Truffer, M. P. Lüthi, M. Fahnestock, M. West, and R. J. Motyka (2008), Glacier, fjord, and seismic response to recent large calving events, Jakobshavn Isbræ, Greenland, *Geophys. Res. Lett.*, *35*(22), L22501, doi:10.1029/2008GL035281.

Amundson, J. M., M. Fahnestock, M. Truffer, J. Brown, M. P. Lüthi, and R. J. Motyka (2010), Ice mélange dynamics and implications for terminus stability, Jakobshavn Isbræ, Greenland, *J. Geophys. Res.*, *115*, F01005, doi:10.1029/2009JF001405.

Amundson, J. M., J. F. Clinton, M. Fahnestock, M. Truffer, M. P. Lüthi, and R. J. Motyka (2012a), Observing calving-generated ocean waves with coastal broadband seismometers, Jakobshavn Isbræ, Greenland, *Ann. Glaciol.*, *53*(60), 79 – 84.

Amundson, J. M., J. C. Burton, and S. Correa-Legisos (2012b), Impact of hydrodynamics on seismic signals generated by iceberg collisions, *Ann. Glaciol.*, *53*(60), 106 – 112.

Bartholomaus, T. C., C. F. Larsen, S. O'Neel, and M. E. West (2012), Calving seismicity from iceberg – sea surface interactions, *J. Geophys. Res.*, *117*, F04029, doi:10.1029/2012JF002513.

Bassin, C., G. Laske, and G. Masters (2000), The current limits of resolution for surface wave tomography in North America, *Eos Trans. AGU*, *81*, F897.

Bouchon, M. (1981), A simple method to calculate Green's functions for elastic layered media, *Bull. Seismol. Soc. Am.*, *71*(4), 959 – 971.

Brodsky, E. E., E. Gordeev, and H. Kanamori (2003), Landslide basal friction as measured by seismic waves, *Geophys. Res. Lett.*, *30*(24), 2236, doi:10.1029/2003GL018485.

Burton, J. C., J. M. Amundson, D. S. Abbot, A. Boghosian, L. M. Cathles, S. Correa-Legisos, K. N. Darnell, N. Guttenberg, D. M. Holland, and D. R. MacAyeal (2012), Laboratory investigations of iceberg capsize dynamics, energy dissipation and tsunamigenesis, *J. Geophys. Res*, *117*, F1007, doi:10.1029/2011JF002055.

Clinton, J. F., et al. (2014), Seismic network in Greenland monitors Earth and ice system, *Eos Trans. AGU*, *95*(2), 13 – 14.

Dziewonski, A., T.-A. Chou, and J. Woodhouse (1981), Determination of earthquake source parameters from waveform data for studies of global and regional seismicity, *J. Geophys. Res.*, *86*(B4), 2825 – 2852.

Ekström, G., M. Nettles, and G. A. Abers (2003), Glacial earthquakes, *Science*, *302*(5645), 622 – 624.

Favreau, P., A. Mangeney, A. Lucas, G. Crosta, and F. Bouchut (2010), Numerical modeling of landquakes, *Geophys. Res. Lett.*, *37*(15), L15305, doi:10.1029/2010GL043512.

Heeszel, D. S., H. A. Fricker, J. N. Bassis, S. O'Neel, and F. Walter (2014), Seismicity within a propagating ice shelf rift: The relationship between icequake locations and ice shelf structure, *J. Geophys. Res. Earth Surf.*, *119*, 731–744.

Howat, I. M., I. Joughin, S. Tulaczyk, and S. Gogineni (2005), Rapid retreat and acceleration of Helheim Glacier, east Greenland, *Geophys. Res. Lett.*, *32*(22), L22502, doi:10.1029/2005GL024737.

Howat, I. M., I. Joughin, and T. A. Scambos (2007), Rapid changes in ice discharge from Greenland outlet glaciers, *Science*, *315*(5818), 1559–1561.

Joughin, I., W. Abdalati, and M. Fahnestock (2004), Large fluctuations in speed on Greenland's Jakobshavn Isbrae glacier, *Nature*, *432*(7017), 608–610.

Joughin, I., I. Howat, R. B. Alley, G. Ekstrom, M. Fahnestock, T. Moon, M. Nettles, M. Truffer, and V. C. Tsai (2008), Ice-front variation and tidewater behavior on Helheim and Kangerdlugssuaq Glaciers, Greenland, *J. Geophys. Res.*, *113*, F01004, doi:10.1029/2007JF000837.

Kawakatsu, H. (1989), Centroid single force inversion of seismic waves generated by landslides, *J. Geophys. Res.*, *94*(B9), 12,363–12,374.

Levy, C., A. Mangeney, F. Bonilla, C. Hibert, E. S. Calder, and P. J. Smith (2015), Friction weakening in granular flows deduced from seismic records at the Soufrière Hills Volcano, Montserrat, *J. Geophys. Res. Solid Earth*, *120*(11), 7536–7557.

Mac Cathles, L., L. Kaluzienski, and J. Burton (2015), Laboratory investigations of seismicity caused by iceberg calving and capsize, Abstract C43B-0803 presented at 2015 Fall Meeting, AGU, San Francisco, Calif., 14–18 Dec.

Moretti, L., A. Mangeney, Y. Capdeville, E. Stutzmann, C. Huggel, D. Schneider, and F. Bouchut (2012), Numerical modeling of the Mount Steller landslide flow history and of the generated long period seismic waves, *Geophys. Res. Lett.*, *39*(16), L16402, doi:10.1029/2012GL052511.

Moretti, L., K. Allstadt, A. Mangeney, Y. Capdeville, E. Stutzmann, and F. Bouchut (2015), Numerical modeling of the mount meager landslide constrained by its force history derived from seismic data, *J. Geophys. Res. Solid Earth*, *120*(4), 2579–2599, doi:10.1002/2014JB011426.

Murray, T., et al. (2015), Reverse glacier motion during iceberg calving and the cause of glacial earthquakes, *Science*, *349*, 305–308.

Nettles, M., and G. Ekström (2010), Glacial earthquakes in Greenland and Antarctica, *Annu. Rev. Earth Planet. Sci.*, *38*(1), 467–491.

Nettles, M., et al. (2008), Step-wise changes in glacier flow speed coincide with calving and glacial earthquakes at Helheim Glacier, Greenland, *Geophys. Res. Lett.*, *35*(24), L24503, doi:10.1029/2008GL036127.

O'Neel, S., H. Marshall, D. McNamara, and W. Pfeffer (2007), Seismic detection and analysis of icequakes at Columbia Glacier, Alaska, *J. Geophys. Res.*, *112*, F03S23, doi:10.1029/2006JF000595.

Peters, I. R., J. M. Amundson, R. Cassotto, M. Fahnestock, K. N. Darnell, M. Truffer, and W. W. Zhang (2015), Dynamic jamming of iceberg-choked fjords, *Geophys. Res. Lett.*, *42*(4), 1122–1129.

Quenouille, M. H. (1956), Notes on bias in estimation, *Biometrika*, *43*, 353–360.

Rial, J., C. Tang, and K. Steffen (2009), Glacial rumblings from Jakobshavn ice stream, Greenland, *J. Glaciol.*, *55*(191), 389–399.

Sergeant, A., V. Yastrebov, O. Castelnau, A. Mangeney, E. Stutzmann, J.-P. Montagner, and J. Burton (2015), Numerical modeling of glacial earthquakes induced by iceberg capsize, Abstract C21A-072 presented at 2015 Fall Meeting, AGU, San Francisco, Calif., 14–18 Dec.

Thomas, R. H., W. Abdalati, T. L. Akins, B. M. Csatho, E. B. Frederick, S. P. Gogineni, W. B. Krabill, S. S. Manizade, and E. J. Rignot (2000), Substantial thinning of a major east Greenland outlet glacier, *Geophys. Res. Lett.*, *27*(9), 1291–1294, doi:10.1029/1999GL008473.

Truffer, M., J. Amundson, M. Fahnestock, and R. J. Motyka (2006), High time resolution velocity measurements on Jakobshavns Isbrae, *Eos Trans. AGU*, *87*(52), Fall Meet. Suppl., Abstract C11A–1132.

Tsai, V. C., and G. Ekström (2007), Analysis of glacial earthquakes, *J. Geophys. Res.*, *112*, F03S22, doi:10.1029/2006JF000596.

Tsai, V. C., J. R. Rice, and M. Fahnestock (2008), Possible mechanisms for glacial earthquakes, *J. Geophys. Res.*, *113*, F03014, doi:10.1029/2007JF000944.

Tukey, J. W. (1958), Bias and confidence in not-quite large samples, *Ann. Math. Stat.*, *29*, 614–614, Inst. Mathematical Statistics Ims Business Office-Suite 7, 3401 Investment Blvd, Hayward, Calif.

Veitch, S. A., and M. Nettles (2012), Spatial and temporal variations in Greenland glacial-earthquake activity, 1993–2010, *J. Geophys. Res.*, *117*, F04007, doi:10.1029/2012JF002412.

Walter, F., J. F. Clinton, N. Deichmann, D. S. Dreger, S. E. Minson, and M. Funk (2009), Moment tensor inversions of icequakes on Gornergletscher, Switzerland, *Bull. Seismol. Soc. Am.*, *99*(2A), 852–870.

Walter, F., S. O'Neel, D. McNamara, W. Pfeffer, J. N. Bassis, and H. A. Fricker (2010), Iceberg calving during transition from grounded to floating ice: Columbia Glacier, Alaska, *Geophys. Res. Lett.*, *37*, L15501, doi:10.1029/2010GL043201.

Walter, F., J. M. Amundson, S. O'Neel, M. Truffer, M. Fahnestock, and H. A. Fricker (2012), Analysis of low-frequency seismic signals generated during a multiple-iceberg calving event at Jakobshavn Isbræ, Greenland, *J. Geophys. Res.*, *117*, F01036, doi:10.1029/2011JF002132.

Walter, F., M. Olivieri, and J. F. Clinton (2013), Calving event detection by observation of seiche effects on the Greenland fjords, *J. Glaciol.*, *59*(213), 162–178.

Wittlinger, G., and V. Farra (2014), Evidence of unfrozen liquids and seismic anisotropy at the base of the polar ice sheets, *Polar Sci.*, *9*(1), 66–79.

Yamada, M., H. Kumagai, Y. Matsushi, and T. Matsuzawa (2013), Dynamic landslide processes revealed by broadband seismic records, *Geophys. Res. Lett.*, *40*(12), 2998–3002.

Yamada, M., A. Mangeney, L. Moretti, and Y. Matsushi (2014), Estimation of dynamic friction process of the Akatani landslide based on the waveform inversion and numerical simulation, Abstract NH14C-08 presented at 2014 Fall Meeting, AGU, San Francisco, Calif., 15–19 Dec.

Zhao, J., L. Moretti, A. Mangeney, E. Stutzmann, H. Kanamori, Y. Capdeville, E. Calder, C. Hibert, P. Smith, P. Cole, and A. LeFriant (2014), Model space exploration for determining landslide source history from long-period seismic data, *Pure Appl. Geophys.*, *172*, 389–413, doi:10.1007/s00024-014-0852-5.